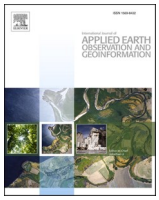
International Journal of Applied Earth Observation and Geoinformation 143 (2025) 104765



Contents lists available at ScienceDirect

International Journal of Applied Earth Observation and Geoinformation

journal homepage: www.elsevier.com/locate/jag





Improving parcel level crop classification by integrating a novel red edge maize-cotton mapping index and machine learning: A case study in the Ebinur Lake Basin

Yan Xie [a,b], Hongwei Zeng [a,b,*], Junbin Li [a,b], Hang Zhao [a,b], Qiangyi Yu [c], Bingwen Qiu [d], Shukri Ahmed [a], Bingfang Wu [a,b,*]

[a] State Key Laboratory of Remote Sensing and Digital Earth, Aerospace Information Research Institute, Chinese Academy of Sciences, Beijing 100101, China
[b] University of Chinese Academy of Sciences, Beijing 100049, China
[c] Key Laboratory of Agricultural Remote Sensing (AGRIRS), Ministry of Agriculture and Rural Affairs/Institute of Agricultural Resources and Regional Planning, Chinese Academy of Agricultural Sciences, Beijing 100081, China
[d] National Engineering Research Centre of Geospatial Information Technology, Key Laboratory of Spatial Data Mining & Information Sharing of Ministry of Education, Fuzhou University, Fuzhou 350002 Fujian, China

ARTICLE INFO

Keywords:
Crop classification
Red Edge Maize-Cotton Index
BFINet
Random forest
Ebinur Lake Basin

ABSTRACT

Accurate crop type classification remains challenged by dependence on ground-based samples and the presence of 'salt-and-pepper' noise. This study presented a hierarchical parcel-level classification framework for multi-crop mapping, integrating the boundary-field interaction network (BFINet), the Red Edge Maize-Cotton Index (RMCI), and a random forest (RF) classifier. BFINet enables precise delineation of agricultural field boundaries, reducing the influence of non-cropland areas and minimizing pixel-level noise. RMCI is a new spectral index designing for maize and cotton classification. The RF classifier is used to separate cropland into dominant crops and minor crops, and subsequently to classify the minor crops into different crops. Applied to 2023 Sentinel-2 imagery in the Ebinur Lake Basin (ELB), the framework produced the region's first detailed crop type map. BFINet delineated agricultural parcels in ELB with IOU of 82.3 % and OA of 87.8 %. RMCI achieved an overall accuracy (OA) of 98.6 % for maize–cotton separation, outperforming RF classifier (98.4 %). For minor crops, the RF model attained an OA of 92.3 %. Compared to directly using standalone RF approach, The hierarchical framework outperformed the standalone RF classifier in classifying all crop types in the ELB with F1 for cotton (99.04 % vs. 87.28 %), maize (97.44 % vs. 96.22 %), wheat–maize (88.2 % vs. 82.0 %), grape (92.7 % vs. 89.0 %), and zucchini (94.4 % vs.75.6 %). This framework offers a scalable and accurate solution for crop mapping in complex agricultural landscapes of arid regions.

1. Introduction

Accurate crop type classification is critical for estimating crop acreage, predicting yields, and supporting agricultural decision-making. In dryland regions, it is also a key prerequisite for estimating agricultural water consumption (Abbasi et al., 2023), balancing agricultural and ecological water consumption, given that agricultural water use is co-determined by both cropland extent and crop type (Zeng et al., 2025). Despite rapid advances in remote sensing and machine learning, three major challenges continue to hinder accurate and timely crop type classification: (1) high dependency on labeled samples, (2) salt-and-pepper noise in classification outputs, and (3) time lags associated with off-season mapping.

Traditional machine learning methods, such as random forests (RF), are widely used for crop classification due to their ability to capture spectral and temporal differences among crops (d'Andrimont et al., 2021; You et al., 2021). Deep learning approaches, including convolutional neural networks (CNNs), long short-term memory (LSTM) networks, and Transformers, have shown great potential in crop classification by extracting complex spatiotemporal patterns from remote sensing data (Zhong et al., 2019). However, both methods rely heavily on large volumes of high-quality labeled data (Kussul et al.,

* Corresponding authors at: State Key Laboratory of Remote Sensing and Digital Earth, Aerospace Information Research Institute, Chinese Academy of Sciences, Beijing 100101, China.
E-mail addresses: zenghw@aircas.ac.cn (H. Zeng), wubf@aircas.ac.cn (B. Wu).

https://doi.org/10.1016/j.jag.2025.104765
Received 1 November 2024; Received in revised form 6 July 2025; Accepted 28 July 2025
Available online 4 August 2025
1569-8432/© 2025 The Authors. Published by Elsevier B.V. This is an open access article under the CC BY-NC license (http://creativecommons.org/licenses/by-nc/4.0/).

2017), which are often costly and labor-intensive to acquire. To address these challenges, two primary strategies have been proposed. The first involves maximizing the utility of limited crop labels (Cai et al., 2024; Xuan et al., 2023), such as leveraging weak supervision and spatio-temporal feature mining to expand limited crop labels (Cai et al., 2024). The second strategy is the development of crop-specific spectral indices, which enable accurate mapping without the need for extensive labeled samples, such as the Cotton Mapping Index (CMI) (Xun et al., 2021), the Variation of the Vegetation-Pigment index (VVP) for maize mapping (Huang et al., 2024), the SAR-based Paddy Rice Index (SPRI)(Xu et al., 2023).

Supervised machine learning-based crop classification often suffers from salt-and-pepper noise due to within-field spectral variability, data missing due to cloud, and interference from adjacent non-crop features (Hirayama et al., 2019; Wang et al., 2024). While post-classification smoothing (Zhu, 2013) and attention-based interpolation for missing data (Wang et al., 2024) can alleviate this problem, more promising results have been achieved using object-based classification, where homogeneous pixels are aggregated into field-level units (Defourny et al., 2019). Nevertheless, such methods require an accurate field boundary delineation task still challenged by complex landscapes and smallholder farming systems. Although deep learning models excel in feature extraction and spatial–temporal context learning, most current architectures perform pixel classification without explicit awareness of field geometry. As a result, they fall short in producing field-aligned and spatially consistent outputs. In practice, agricultural decision-making operates at the field or parcel level, underscoring the need for parcel-aware classification. Recent advances in deep learning–based segmentation models, such as BsiNet (Long et al., 2022; Zhao et al., 2024), SEANet (Li et al., 2023), HBGNet (Zhao et al., 2025), have shown promising results in extracting field boundaries. Nonetheless, challenges persist in fragmented and smallholder farming areas, where fields are small and boundaries are often irregular or poorly defined.

Timeliness is another major challenge. Most existing crop maps are generated in the post-harvest season due to the scarcity of reliable in-season labels and the underuse of crop phenological characteristics (Zhang et al., 2022). This stems from difficulties in acquiring reliable in-season labels and limited integration of crop phenology (Worrall et al., 2023). To address this, recent studies have leveraged phenological insights and deep learning techniques to enable in-season classification. For instance, You et al. (2021) employed a hierarchical approach that utilizes crop-specific phenological variations. Wang et al. (2023) developed the Deep Adaptation Crop Classification Network (DACCN) to enhance cross-domain transferability. More recently, Zhang et al. (2024) developed Mask-PSTIN, a framework that combines temporal random masking and pixel-set aggregation to improve model robustness and early-season classification under limited and noisy observations.

These challenges are further amplified in multi-crop and water-limited regions, where diverse crop phenology, fragmented field structures, and environmental variability exacerbate classification uncertainty. No single approach can fully address these complexities. Therefore, an integrated and scalable framework that leverages spectral and phenological information, improves field-level spatial consistency, and reduces dependence on extensive labeled data is urgently needed.

This study proposes a integrating framework tailored to the Ebinur Lake Basin (ELB), a key arid agricultural region in Xinjiang, China experiencing increasing water stress due to irrigated agriculture expansion and cotton cultivation (Zeng et al., 2025). Despite several land use studies in the ELB (Ma et al., 2020), detailed crop type data remain scarce, limiting the assessment of agricultural water impacts. Our objectives are: (1) design a hierarchical approach to combine crop phenology, index-based and machine learning-based methods to reduce dependence on labeled data and enhance classification accuracy; (2) integrating high-precision field parcel delineation to mitigate salt-and-pepper noise; (3) generating high-resolution crop type data to address data gaps, thereby improving the assessment of agricultural impacts on water consumption in the ELB.

2. Materials

2.1. Study area

The ELB, situated in the northern foothills of the Western Tianshan Mountain of China, mainly include Bole, Jinghe, Wenquan, Wusu, Tori, as well as the Ebinur Lake Wetland National Nature Reserve. The latitudes spanned from 43°37′N to 45°53′N and longitudes spanned from 79°52′E to 85°16′E. The climate is dominated by temperate continental climate, characterized by an average annual temperature of 7.8 °C and low annual precipitation ranging from 89.8 mm to 169.7 mm. As a key ecological barrier and major agricultural region in northern China, the ELB faces increasing water stress driven by expanding irrigated agriculture and cotton cultivation (Zeng et al., 2025). Although several studies have investigated land use and land cover changes in the ELB (Ma et al., 2020), few have focused on crop type classification. However, the scarcity of detailed crop type data limits a comprehensive understanding of agriculture's impact on water resources in the ELB.

Maize, cotton, winter wheat, silage maize, and other crops are widely cultivated in the ELB. Their phenological calendar is shown in Fig. 2. Major crops include maize, cotton, winter wheat, and silage maize, whose phenological calendars overlap notably, especially between spring maize and cotton during mid-summer—causing spectral confusion in classification. Additionally, double cropping systems of winter wheat-silage maize further complicate crop mapping (Zhang et al., 2013).

2.2. Data

Sentinel-1/2 imagery, crop labels data, and auxiliary datasets were utilized to design hierarchical classification strategy for multi-crop type mapping of ELB in 2023.

2.2.1. Satellite data and processing

The satellite data included Sentinel-2 (S2) Multispectral Instrument (MSI) Level-2A data and Sentinel-1 C-band Synthetic Aperture Radar Ground Range Detected products (S1 SAR GRD) in 2023.

(1) Sentinel-2 satellite data

The cloud probability was used to mask clouds and cloud shadows in S2 imagery. Ten spectral bands from S2, spanning from the blue to the SWIR2 band, were selected for spatial feature engineering. To ensure temporal consistency, 15-day composite images were generated by calculating the median of all valid observations within each 15-day interval. To further enhance the quality of the time series and remove outliers, a Savitzky-Golay (SG) filter with a 9-point window and second-order polynomial fitting was applied.

In addition, ten indices (Table 1) were calculated to support crop identification based on the characteristics of dominant crop, cotton, in the ELB. (1) Several commonly used indices—BSI, EVI, NDVI, NDSI, LSWI, MCARI, NDRI, and PSRI—have been widely applied for cotton mapping (Tian et al., 2023; Xun et al., 2021); (2) The Normalized Difference Red Edge Index (NDRE), which is highly sensitive to chlorophyll content, can capture the grayish-white visual appearance of cotton during the boll-opening stage (Sims and Gamon, 2002); (3)The Enhanced Bloom Index (EBI), originally developed to quantify almond blossom phenology (Chen et al., 2019), was incorporated as the gray-white reflectance characteristics of almond blossoms are spectrally similar to those of open cotton bolls.

Texture information has been shown to be valuable for crop type classification. Kang et al. (2023) evaluated the performance of 18 texture features using 'glcmTexture' function in the Google Earth Engine (GEE) (Gorelick et al., 2017) for cropland extraction and cotton

Table 1
The vegetation indices along with their corresponding formulas based on Sentinel-2 spectral bands.

Spectral index	Expression	Reference
BSI: Bare Soil Index	$\frac{(B11+B4)-(B8+B2)}{(B11+B4)+(B8+B2)}$	Diek et al. (2017)
EVI: Enhanced Vegetation Index	$2.5\times\frac{(B8-B4)}{(B8+6\times B4-7.5\times B2+1)}$	Huete et al. (2002)
NDVI: Normalized Difference Vegetation Index	$\frac{B8-B4}{B8+B4}$	Fung and Siu (2010)
NDSI: Normalized Difference Soil Index	$\frac{B11-B8}{B11+B8}$	Deng et al. (2015)
LSWI: Land Surface Water Index	$\frac{B8-B11}{B8+B11}$	Xiao et al. (2010)
NDRE: Normalized Difference Red Edge Index	$\frac{B8-B6}{B8+B6}$	Sims and Gamon (2002)
MCARI: Modified Chlorophyll Absorption Ratio Index	$(B5-B4)-0.2\times(B5-B3)\times(B5/B4)$	Wu et al. (2008)
PSRI: Plant Senescence Reflectance Index	$\frac{B4-B2}{B6}$	Merzlyak et al. (2002)
NDRI: Normalized Difference Residue Index	$\frac{B4-B12}{B4+B12}$	Nagler et al. (2000)
EBI: Enhanced Blossom Index	$\frac{B2\times(B2+B3+B4)}{B2\times(B4-B2+1)}$	(Chen et al., 2019)

Note: Specifically, B2, B3, B4, B5, B6, B8, B11, and B12 represent the blue, green, red, red edge 1, red edge 2, near-infrared (NIR), shortwave infrared 1 (SWIR1), and shortwave infrared 2 (SWIR2) bands, respectively.

identification. They found that the sum average (SAVG, Eq. (1)) derived from the S2 blue band outperformed other texture metrics. This finding aligns with earlier results by Shafizadeh-Moghadam et al. (2021). Based on this evidence, the SAVG of the S2 blue band was selected to enhance crop type classification.

$$SAVG=\sum_{k=2}^{2N_g}k\left(\sum_{i=1}^{N_g}\sum_{j=1}^{N_g}p(i,j)\right),i+j=k \quad (1)$$

where, $p(i,j)$ represents the (i, j)th entry in the Gray-Level Co-occurrence Matrix (GLCM) of a pixel, and N_g denotes the number of distinct gray levels in the quantized image. For each GLCM, the neighborhood size was set to 4, with a 9 × 9 kernel (radius = 4 pixels).

(2) Sentinel-1 satellite data

Previous studies have demonstrated that radar backscatter coefficients effectively capture crop structure characteristics, ground condition, and their interaction (Veloso et al., 2017). Here, S1 SAR GRD imagery acquired in interferometric wide swath mode was used for crop type classification. To reduce speckle noise, the Refined Lee filter with a 7 × 7 window was applied. The SAR images were composited at 15-day intervals by calculating the median value of all observations within each period and subsequently converted to decibel (dB) units using the formula 10 × log10(×) (Mullissa et al., 2021). To further enhance the time series quality, SG filter with a 7-point window and second-order polynomial fitting was employed for additional noise reduction.

2.2.2. Crop geo-referenced points and agricultural parcels

Crop labels were collected in September 2023 using the GPS-Video-GIS (GVG) app (Wu and Li, 2012). A total of 6997 geo-referenced points (Fig. 1) were collected, including cotton, wheat, maize, and various other crops (grapes, zucchini, and others). Specifically, the labeled samples included 4206 cotton, 1696 maize, 175 winter wheat–silage maize (wheat-maize), 407 grape, 245 zucchini, and 268 other crops. To support framework designed, the samples were divided into three groups: the balanced sample set (SP_b), the full sample set of cotton and maize (SP_{cm}), the full sample set of other crops (SP_o). SP_b comprised 300 randomly selected samples each for cotton and maize, and 600 for minor crops. SP_{cm}, SP_o, and SP_b were stratified and randomly split into a training set (70 %) and a validation set (30 %). In addition, 476 agricultural parcels were manually delineated through visual interpretation to validate the parcel delineation results generated by BFINet model.

2.2.3. Auxiliary data

To eliminate the influence of non-cultivated land in crop classification, the cropland layer from the ChinaCover2020 (Wu et al., 2024), a land cover data developed by the Chinese Academy of Sciences was utilized. This product has a spatial resolution of 10 m and an OA of 91 %, derived from high-resolution remote sensing imagery. Originally developed for ecosystem assessments, the cropland layer includes some non-cropland features, such as field roads and ridges. Therefore, further cleaning is needed to get a more accurate cropland map.

3. Methods

The workflow of the hierarchical parcel-level approach for multi-crop classification is illustrated in Fig. 3. First, the BFINet was employed to delineate agricultural field boundaries from the cropland layer of ChinaCover2020. Based on these field parcels, a hierarchical crop type classification strategy was designed to improve crop type discrimination. In the first step, an RF classifier was employed to separate the cropland into two groups: dominant crops (maize and cotton) and minor crops (grape, zucchini, and others). In the second step, a new Red Edge Maize-Cotton Index (RMCI) was developed to differentiate maize and cotton by analyzing spectral bands with high separability. Simultaneously, the RF classifier was further applied to classify the minor crops into specific crop types. Finally, the classification results from both groups were merged to produce comprehensive spatial distribution map of crop types in the ELB.

3.1. BFINet for boundary delineation

BFINet (Zhao et al., 2024) is dual-branch architecture designed for high-precision delineation of agricultural field parcels. It was originally trained on irregular and smaller field in the Chongqing and Hunan province of China, where the IOU and OA were 83.3 % and 89.7 %, respectively. In this study, BFINet was implemented on a local workstation equipped with an NVIDIA RTX 3080 GPU (10 GB VRAM), 32 GB RAM, and 1 TB of storage.

BFINet jointly learns semantic features of both field boundaries and masks, enabling more accurate field delineation. It consists of three key modules: (1)semantic interaction module, which enables weight sharing between the boundary and field mask tasks, improving field identification accuracy; (2) boundary enhancement module, which refines spatial details to enhance boundary delineation precision; and (3) multi-scale module, which employs convolution kernels of varying sizes to capture global and local field features, improving the delineation of fields with different sizes and shapes.

3.2. Classifier for classification

The RF classifier was selected as benchmark classifier to separate cropland into two groups: dominant crops and minor crops, and subsequently to classify the minor crops into wheat–maize, zucchini, grape, and other categories. RF is widely used in crop classification tasks due to its robustness, non-parametric nature, and ease of implementation (Altman and Krzywinski, 2017). As an ensemble classifier, RF combines multiple decision trees to improve predictive accuracy, making it a reliable and widely adopted method in crop type classification.

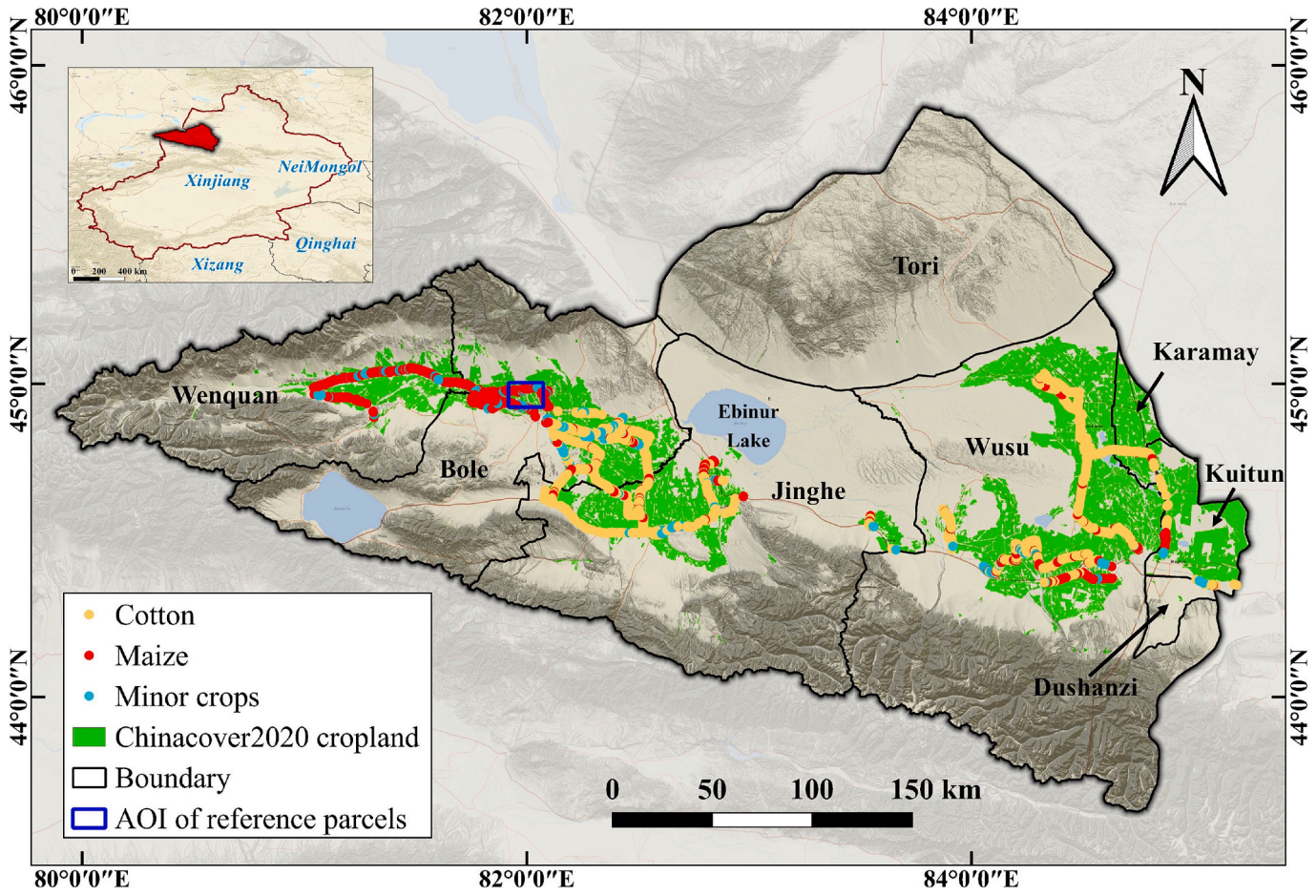


Fig. 1. The geographical location of ELB and distribution of crop samples collected during field surveys.

	Apr			May			Jun			July			Aug			Sep			Oct		
	E	M	L	E	M	L	E	M	L	E	M	L	E	M	L	E	M	L	E	M	L
Cotton		Sowing stage		Seedling stage					Bud stage		Blossoming and boll forming stage				Boll opening stage						
Spring maize			Sowing stage		Seedling stage			Jointing stage		Tasseling stage				Milk stage			Mature stage				
Winter wheat		Jointing stage		Heading stage			Milk stage		Mature stage												
Silage maize									Sowing and seedling stage			Jointing and Tasseling stage			Silking and milk stage			Mature stage			

Fig. 2. Phenological calendar of major crops in the ELB.

Following the recommendation of You et al. (2021), the number of decision trees was set to 120, and the minimum number of samples required to form a leaf node was set to 10. In addition, Support Vector Machine (SVM) and Gradient Tree Boosting (GTB) classifiers were employed to compare the performance with RF.

3.3. RMCI for classification of cotton and maize

To reduce crop labels dependent, RMCI was newly proposed to separate maize and cotton in the ELB using a combination of phenological analysis, feature analysis, and mathematical method.

3.3.1. Phenological analysis for optimal classification time window

To better capture the distinct temporal characteristics of different crop types, this study divided the growing season into early growing season (EGS), peak growing season (PGS), and late growing season (LGS) (Lian et al., 2021). Here, the green chromatic coordinate (GCC) (Shen et al., 2022; Sonnentag et al., 2012) was utilized to determine growing season and the optimal time window. Spectral analysis conducted by GCC can reveal inconsistencies in the timing of peak occurrences and the steepness of the time-series profile for different crops. Phenological analysis use GCC to reveal variability in the timing of peak vegetation activity and the slope of the temporal profile among crops (Shen et al., 2022). The growing stages of crops can be identified by the

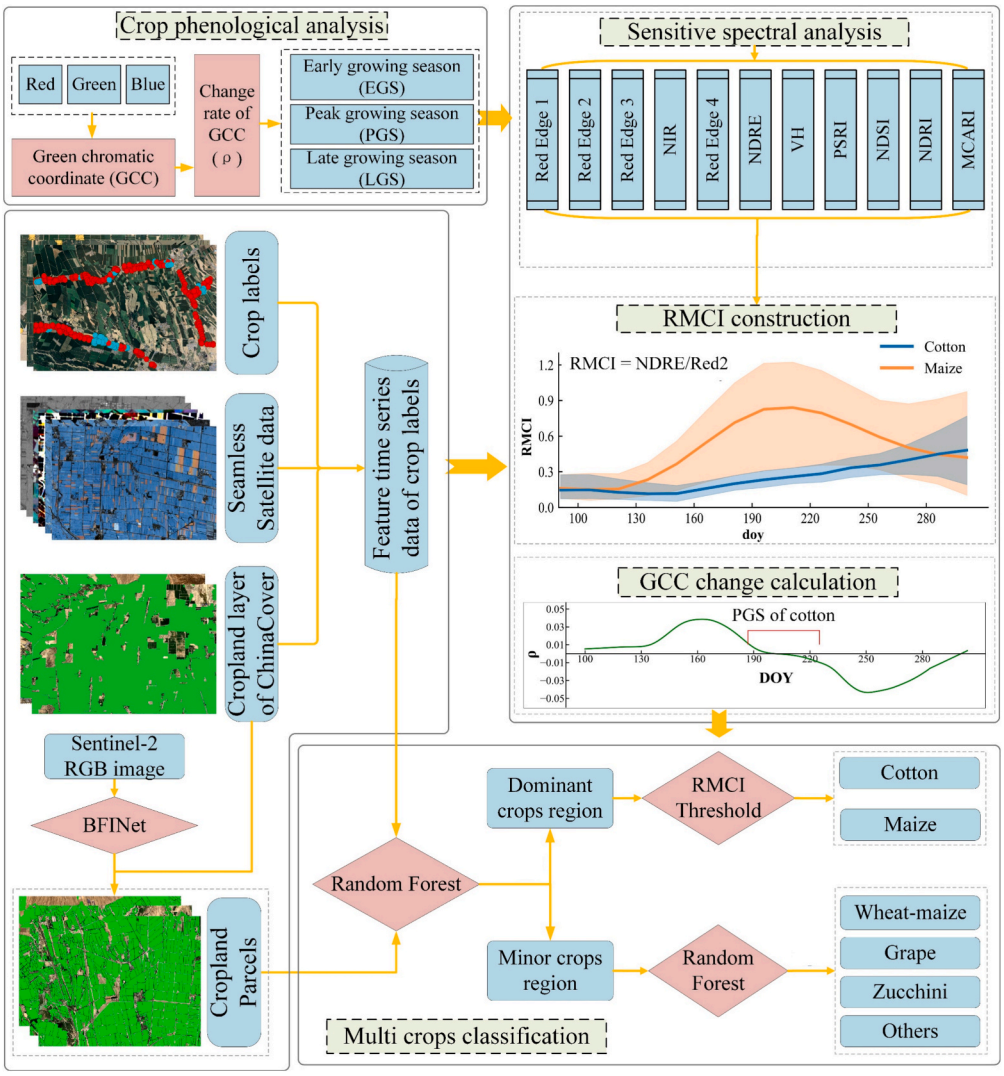


Fig. 3. Hierarchical parcel-level workflow for multi-crop classification in ELB.

rate of GCC (ρ_t). GCC values increase progressively during crop germination and growth, then stabilize once the canopy reaches full development, with only minor fluctuations in ρ_t during this phase, and then subsequently decline during senescence. The definition of GCC and ρ_t are shown as follows:

$$GCC = \frac{G}{R+G+B} \tag{2}$$

$$\rho_t = \frac{GCC_t - GCC_{t-1}}{GCC_{t-1}} \tag{3}$$

where R, G, and B were the values of the red, green, and blue spectral bands, respectively. The variable t represented the specific date, with GCC_t and GCC_{t-1} denoting the GCC value at date t and (t-1), respectively. The ρ_t represented the rate of change of GCC at date t. The EGS, PGS, and LGS of cotton can be identified by the variation in ρ (Chen et al., 2019). Specifically, the EGS was characterized by ρ values exceeding 0.01. The PGS was marked by ρ values ranging between –0.01 and 0.01. The LGS was defined as the period from PSG to the occurrence of a negative peak in ρ, indicating the onset of crop senescence.

3.3.2. *The identification of optimal feature for dominant crops separation*

To identify highly discriminative features capable of effectively distinguishing maize and cotton in the ELB, a detailed analysis was conducted on the dynamic trends of various reflectance bands, vegetation indices, and texture features throughout the growing season, as represented by changes in day of year (DOY) (Fig. 4).

Our analysis found that the red edge 2 (hereafter Red2) band, NDRE and VH exhibited the highest discriminability between maize and cotton, with Jeffries-Matusita (JM) distance equals to 0.712, 0.574, and 0.326. The notably difference of Red2 and VH between cotton and other crops aligns with the findings of Xun et al. (2021), who also declared both are suitable to differentiate cotton from non-cotton features. The discriminative ability of VH was previously employed by Kang et al. (2023) for cotton mapping. However, the potential of NDRE for cotton identification has not yet been fully explored.

3.3.3. *The mathematical expression of RMIC*

Further analysis of the spectral characteristics of maize and cotton revealed that the absolute difference between the Nir and Red2 bands was not sufficiently distinct during the PGS of cotton. However, the distinction in NDRE primarily arose from the sum of the Nir and Red2 band values. To enhance the separability between maize and cotton, both the NDRE and Red2 bands at PGS of cotton were employed to construct the RMCI. The definition is as follows:

$$RMCI = \frac{NDRE}{Red2} \tag{4}$$

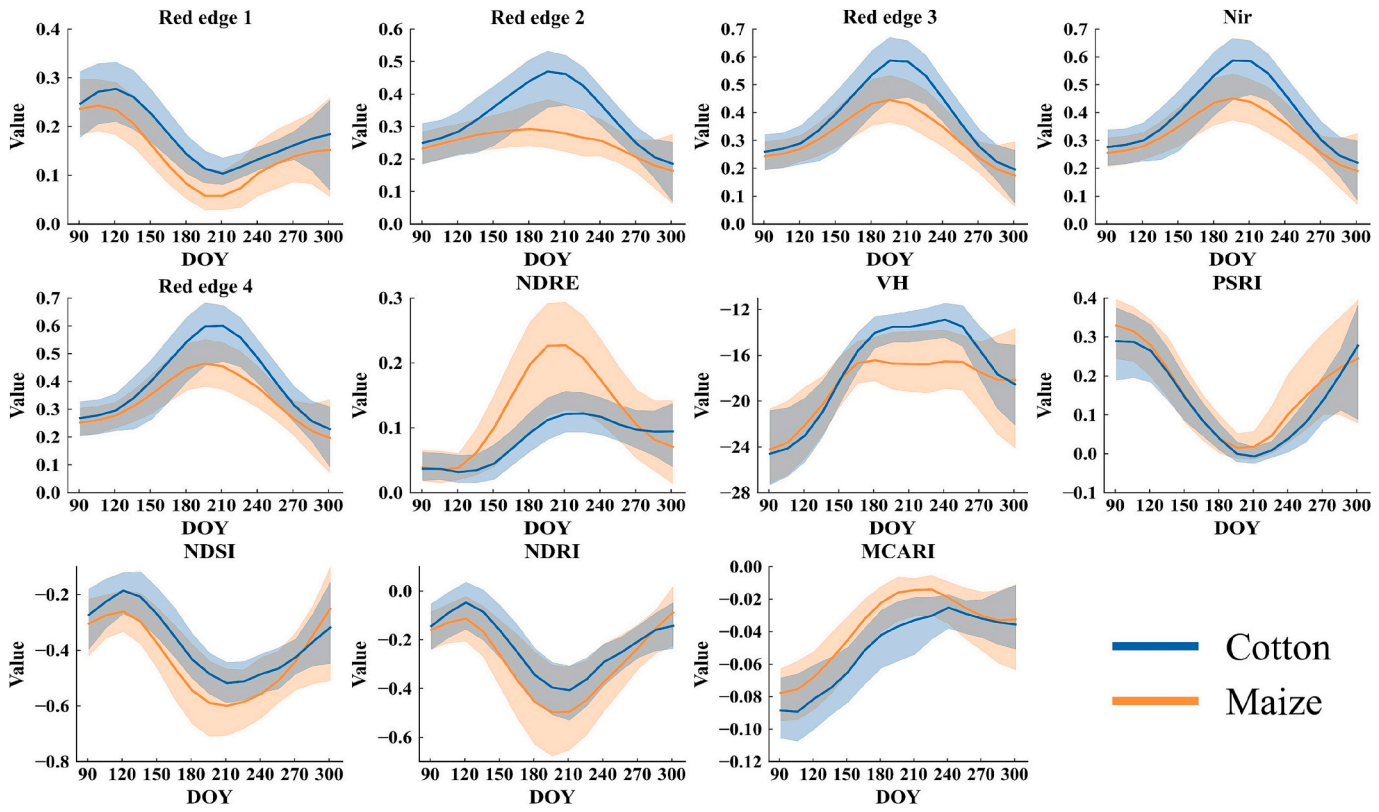


Fig. 4. Feature evaluation for high separability between Maize and Cotton. Shaded areas represent the 5th to 95th percentile range of variation within each class.

Fig. 5 illustrates ρ of the GCC alongside the temporal variation of RMCI. The EGS of cotton occurred between DOY 140 and 180, the PGS spanned DOY 180 to 220, the LGS is from DOY 220 to the onset of crop senescence. During the PGS, the RMCI exhibited the greatest separability between maize and cotton, with higher contrast compared to the EGS and LGS.

To determine the optimal RMCI threshold for distinguishing maize and cotton, we employed a threshold-based classifier and applied GridSearchCV method from the sklearn library (Pedregosa et al., 2011), a widely used method for parameter tuning and threshold optimization (Zhang et al., 2023). Using a validation sample set of SP_{cm} during the PGS, candidate thresholds ranging from 0.1 to 0.6 (at 0.01 intervals) were evaluated. The threshold that yielded the highest overall accuracy (OA) was selected as the final decision criterion.

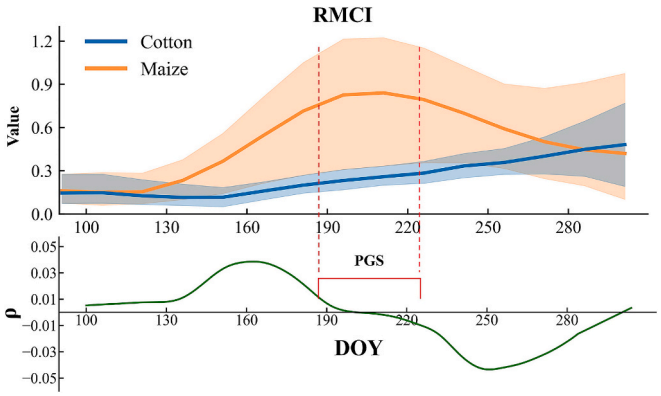


Fig. 5. Temporal profile of GCC rate of change and RMCI, with shaded areas representing the 5th to 95th percentile range of RMCI values for maize and cotton.

3.4. Method of accuracy assessment and post-processing

The accuracy of crop type mapping was quantitatively evaluated using OA, producer accuracy (PA), user accuracy (UA), F1-scores (F1), Kappa coefficient, and intersection over union (IOU). The IOU formula is given as follows:

$$IOU = \frac{TruePositive}{TruePositive + FalsePositive + FalseNegative} \quad (5)$$

where *True Positive, False Positive and False Negative* denote the number of true positive, false positive and false negative pixels, respectively.

To mitigate the 'salt-and-pepper' noise in pixel-level classification results, a "despeckling" algorithm was applied (Deines et al., 2019). For patches smaller than 0.25 ha, classification results were refined using a majority filter with a 20-meter square kernel. The 0.25 threshold was set based on field size in the ELB. The post-processing strategy effectively reclassified most isolated pixels as background and filled small gaps within the cotton fields (Tian et al., 2023).

4. Results

4.1. Delineation of cropland parcels in the ELB

We directly applied the pretrained BFINet model to the ELB without additional fine-tuning. Inference on a single remote sensing image of the specified size from the ELB took approximately 2 h. Compared with 476 manually delineated reference parcels, the BFINet model achieved high accuracy with an IOU of 82.3 % and OA of 87.8 % (Fig. 6). These results highlight the strong robustness and spatial transferability of the BFINet model, pretrained on regions characterized by small and irregular field patterns, enabling accurate cropland parcel delineation in the ELB.

The delineated cropland parcels of ELB and their differences from the cropland layer of ChinaCover2020 were shown in Fig. 7. The average field size ranged from 0.09 ha to 2.90 ha, with a mean parcel size of 0.64

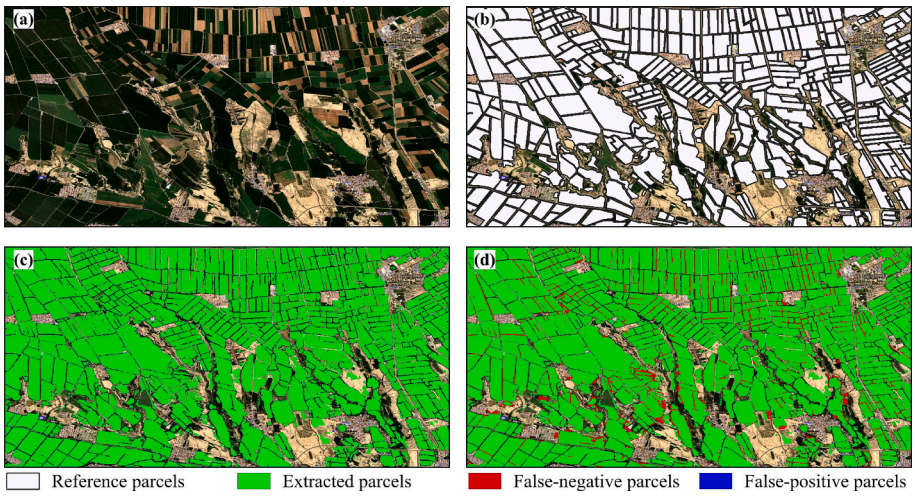


Fig. 6. Comparison of agricultural parcels between reference field and BFINet delineation.

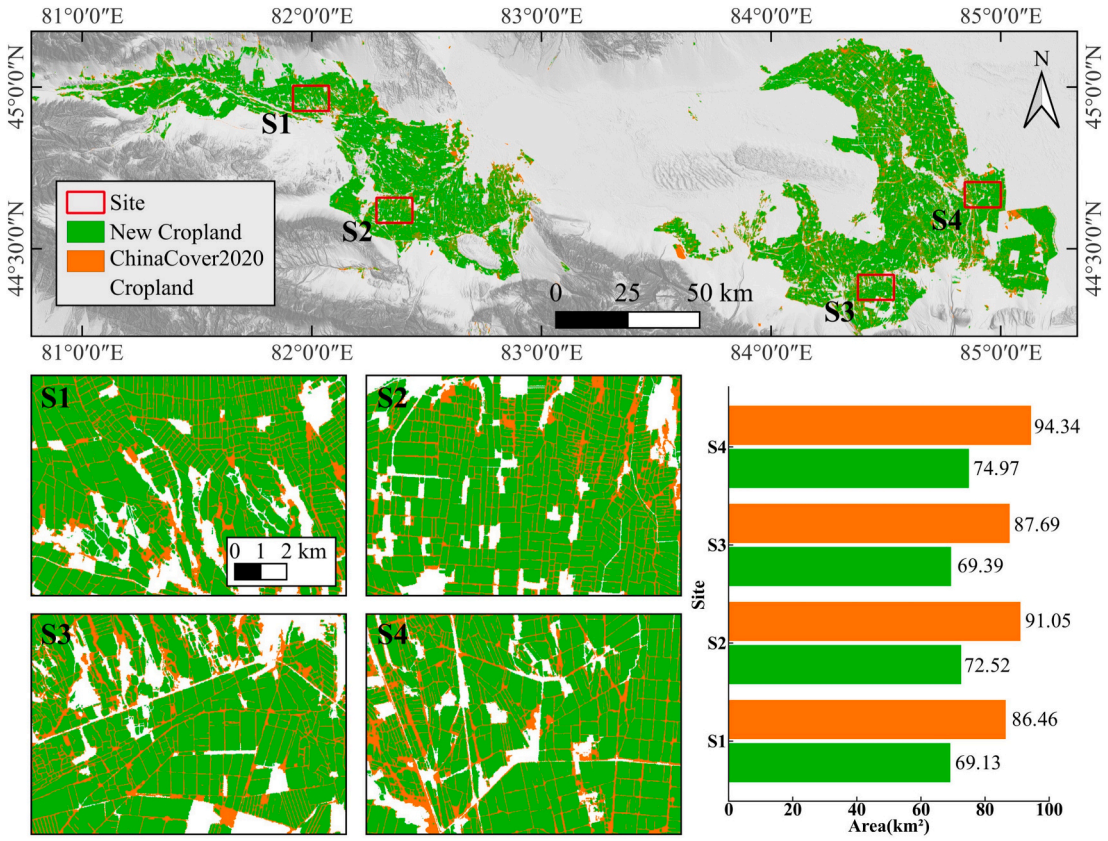


Fig. 7. Delineation of cropland parcels of ELB and comparison with cropland layer of ChinaCover2020.

ha. The BFINet-derived cropland mask effectively suppressed noise from non-cropland features (e.g., field roads), which were commonly misclassified as cropland in ChinaCover2020. Area comparison revealed that ChinaCover2020 overestimated cropland extent by approximately 26 %.

4.2. Classification of dominant and minor crop groups

The spatial distribution of dominant and minor crops group generated using SP2 samples and RF classifier was presented in Fig. 8. The RF model achieved an OA of 96.15 %, with a Kappa coefficient of 0.922, PA, UA, and F1 all exceeding 94 % based on validation sample. The spatial distribution across the four subregions (S1, S2, S3, S4) showed clear boundaries with minimal 'salt-and-pepper' noise, benefiting from the delineated agricultural parcels. The total area covered of dominant crops was 4326.65 km^2, while minor crops covered approximately 1286.51 km^2.

In addition, we evaluated the performance of SVM and GTB classifiers for distinguishing dominant and minor crops. SVM achieved an OA of 50.80 % with a kappa coefficient of 0.02, while GTB yielded an OA of 95.67 % and a kappa of 0.91. Both methods underperformed compared to the RF classifier in the classification of dominant and minor crops within the ELB. Therefore, RF was selected as the benchmark method for this task.

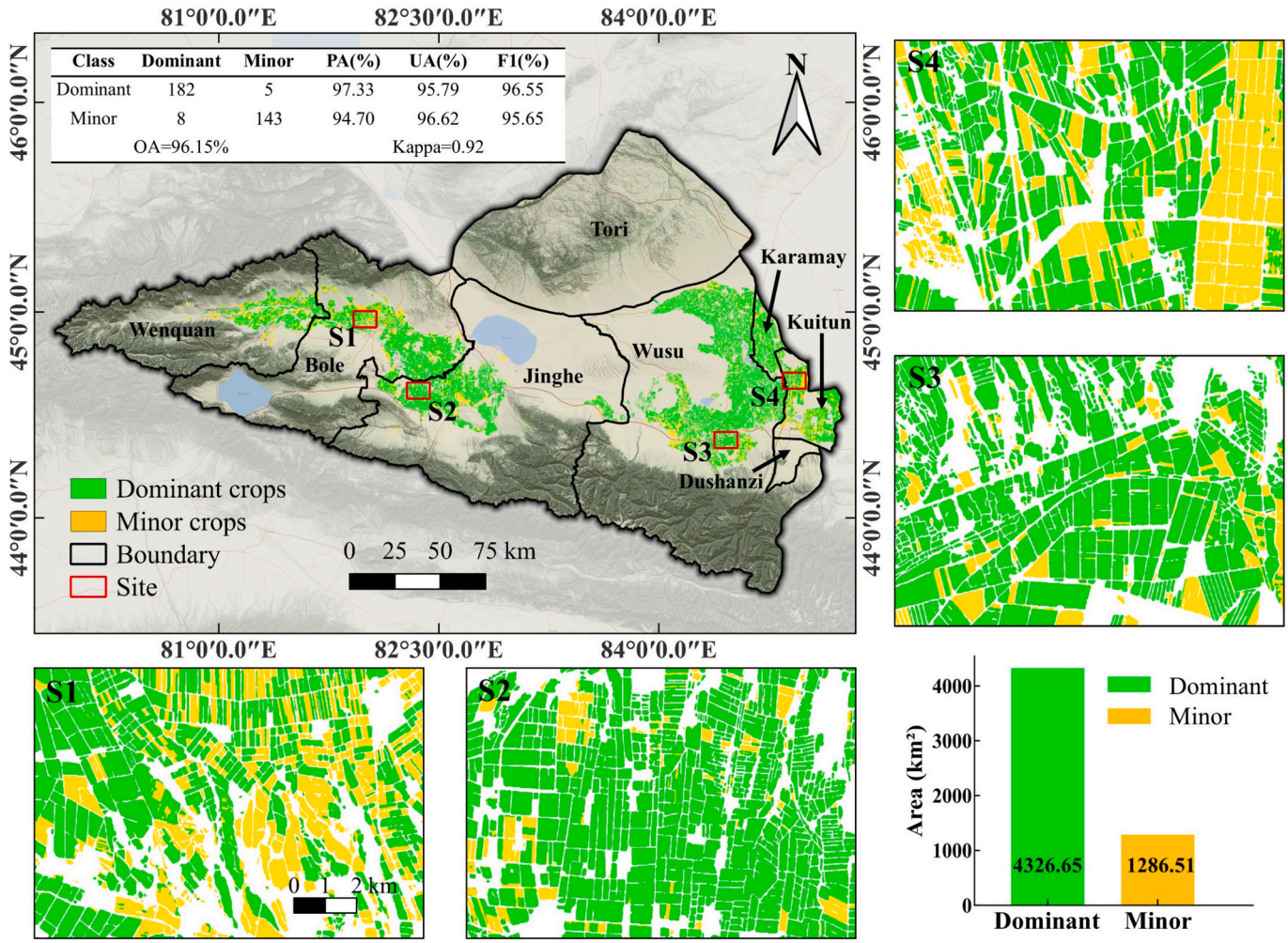


Fig. 8. Classified results of dominant crops and minor crops in the ELB for 2023.

4.3. Separation of maize and cotton

The optimal RMCI threshold during the PGS period of cotton in 2023 was estimated to be 0.42 using GridSearchCV method. This optimized threshold was then applied to distinguish maize from cotton within the dominant crops group. The spatial distribution of true color images, RMCI and classified result of maize and cotton of four subregions (S1, S2, S3, and S4 in Fig. 7) were shown in Fig. 9. The average RMCI values during the PGS demonstrated a clear separation between maize and cotton, with higher RMCI values corresponding to maize and lower values indicating cotton.

A stratified random sampling approach using 30 % of maize and cotton samples from SP1 was employed to calculate the accuracy by RMCI (Table 2). The OA reached 98.60 %, the F1 of maize and cotton were 99.04 % and 97.44 %, PA and UA for both crops exceeding 94 %. These high metric values clearly demonstrate the effectiveness of RMCI in distinguishing between maize and cotton.

We compared RMCI with RF classifier that was trained with nearly 3000 cotton samples and 1100 maize samples (Fig. 10). The spatial distribution of both showed high agreement, with only minor differences observed within the highlighted black circle. The RMCI threshold method showed slightly higher accuracy than RF classifier, with the OA increasing from 98.4 % to 98.6 %, and minimal differences in area statistics. The RMCI method estimated cotton and maize areas at 3,534.39 km^2 and 787.74 km^2, respectively, compared to 3,505.89 km^2 and 816.24 km^2 for the RF classifier. These results underscore the robust performance of RMCI in effectively distinguishing between maize and cotton.

4.4. Minor and final crop type classification result

Within the minor regions, 70 % of samples from the minor crops group in SP1 were used with RF classifier to classify wheat-maize, zucchini, grapes, and other crops. As shown in Table 3, the accuracy assessment indicated an OA of 92.28 %, with PA, UA, and F1 for all crop types exceeding 88 %. Notably, the classification accuracy of RF classifier for minor crops was lower than that for dominant crops, especially, wheat-maize exhibiting the lowest accuracy (PA = 88.24 %, UA = 88.24 %, and F1 = 88.24 %), some of them were mixed with grapes. In addition, grapes were also mixed with zucchini and wheat-maize. The mixed issue is primarily attributed to insufficient crop labels.

We also tested SVM and GTB classifiers in the classification of minor crops. SVM achieved an OA of 41.40 % with a kappa coefficient of 0.05, while GTB yielded an OA of 93.10 % with a kappa of 0.91. Both methods underperformed compared to the RF classifier in the classification of minor crops within the ELB. Consequently, RF was adopted as the benchmark method for minor crop classification as well.

The final crop classification result of ELB in 2023 was generated by combining maize, cotton, wheat-maize, zucchini, grapes, and other crops. The overall ELB classification results, along with detailed maps of the sub-regions S1-S4, were presented in Fig. 11. All crops were shown in the result with clear field boundaries minimal ‘salt-and-pepper’ noise. Overall, cotton, maize and wheat-maize were classified with high accuracy, while grapes and zucchini were also effectively distinguished. In

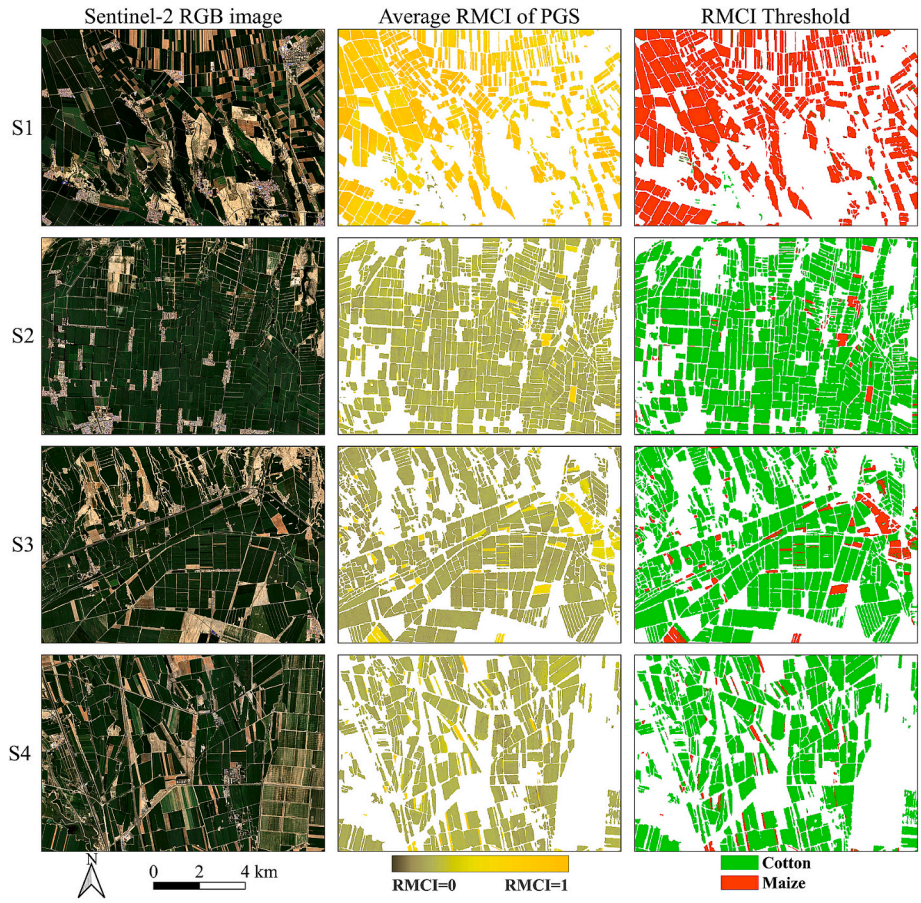


Fig. 9. The spatial distribution of the RMCI values and the classification results by RMCI. From left to right: sentinel-2 RGB image, average RMCI during the PGS, and RMCI-based classification results.

Table 2
Accuracy of RMCI-based crop classification within dominant crop groups.

Crop group	Class	Cotton	Maize	PA (%)	UA (%)	F1 (%)
Dominant	Cotton	1079	7	99.36	98.72	99.04
	Maize	14	399	96.61	98.28	97.44
	OA = 98.60 %			Kappa = 0.9647		

the ELB, the proportion of each crop type was as follows: cotton (64.43 %), maize (14.36 %), wheat-maize (6.67 %), zucchini (8.37 %), grapes (3.43 %), and others (2.74 %). Their spatial distribution showed clear heterogeneity, largely shaped by variations in temperature, water availability, and agricultural practices. Cotton was primarily cultivated in the eastern areas, whereas maize was mainly grown in the western regions of ELB.

Detailed classification results were observed across subregions S1 to S4. In S1, the main crops were maize and wheat–maize, and minor crops like grapes and zucchini were also well distinguished. In S2, cotton was the dominant crop and clearly identified. Grapes were well separated, but some confusion occurred between zucchini and other crops (black circle). In S3, cotton remained the dominant and well-classified crop, though slight confusion was observed between spring maize and zucchini (red circle). In S4, cotton and grape were the main crops and both were accurately classified, with minor misclassification between grape and zucchini (red circle).

5. Discussion

This hierarchical crop classification framework combines index-based and machine learning methods for multi-crop mapping at parcel level. It reduces reliance on crop labels and mitigates 'salt-and-pepper' noise while maintaining high classification performance. The newly proposed RMCI effectively distinguishes maize and cotton in the ELB. Moreover, the generated crop type data help fill a critical information gap in the ELB, supporting better agricultural water management in a region with strong conflict between farming and ecological protection.

5.1. The advantage of the hierarchical classification strategy for multi-crops classification

To evaluate its effectiveness of hierarchical classification strategy, its results were compared with were compared with those obtained using only the RF classifier. First, the hierarchical approach by integrating agricultural parcels notably reduced the 'salt and pepper' noise common in pixel-based classifications. Second, it achieved strong classification performance. F1 for various crops were shown in Table 4. The results showed that the hierarchical classification approach outperformed the standalone RF classifier for all crops, with particularly lower accuracy observed for minor crops when using RF alone compared to the hierarchical strategy. This discrepancy was primarily due to the RF tendency to overfit the dominant crops and underfit the minor crops when classifying multiple crops simultaneously, especially when the crop labels of dominant crops far outnumber minor crops. A similar issue was reported by Zeng et al. (2020), who also observed this phenomenon of imbalanced performance when dealing with datasets dominated by major landcover. The superior performance of the hierarchical strategy has also been highlighted in previous studies (Asadi and Shamsoddini, 2024; Tan et al., 2011), largely due to its ability to mitigate class interaction effects (Yang et al., 2023).

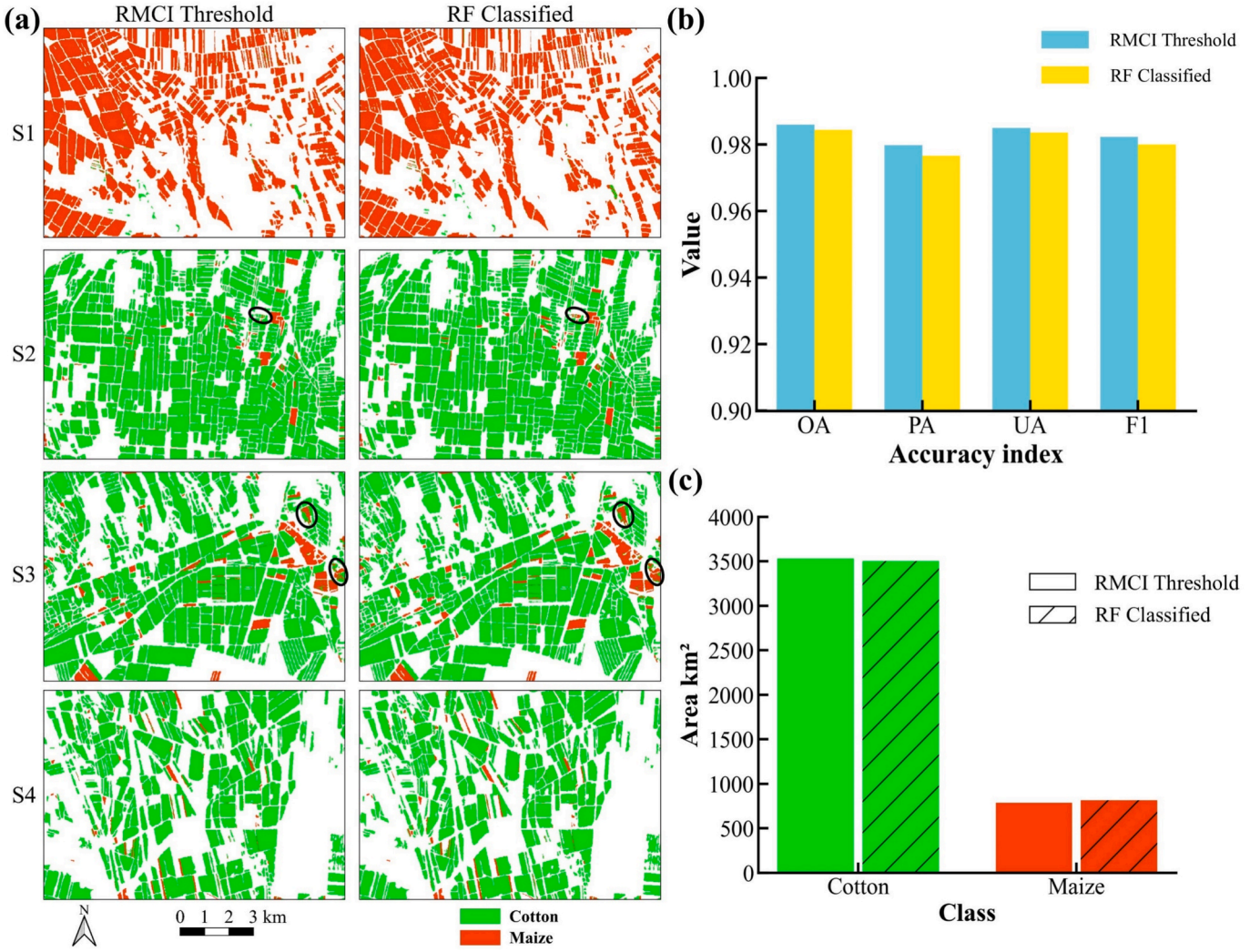


Fig. 10. Comparison of RMCI threshold and RF classifier in 4 subregions for cotton and maize. Spatial distribution of cotton and maize in sub-regions (a), accuracy evaluation of both methods (b), area comparison of both methods (c).

Table 3
Overview of minor crop classification accuracy.

Crop group	Class	Wheat-maize	Grape	Zucchini	Others	PA (%)	UA (%)	F1 (%)
Minor	Wheat-maize	30	4	0	0	88.24	88.24	88.24
	Grape	2	101	1	0	97.12	88.60	92.66
	Zucchini	0	3	42	1	91.30	97.67	94.38
	Others	2	6	0	54	87.10	98.18	92.31
	OA = 92.28 %				Kappa = 0.8890			

5.2. *Why RMCI is good for the separation of maize and cotton*

The JM for the RMCI is 0.751, surpassing that of the NDRE (0.574) and the Red2 band (0.712), indicating that RMCI offers the strongest spectral separability between maize and cotton. This advantage arises from the distinct physiological and spectral dynamics of the two crops. As maize develops from the seedling stage to maturity, leaf chlorophyll content increases notably, and the cellular structure becomes progressively denser. These change result in higher red-edge reflectance and diminished red reflectance (Pagani et al., 2009). Conversely, cotton exhibited a continuous increase in Red2 band reflectance prior to boll opening (Hong et al., 2022; Shi et al., 2022). NDRE, derived from the NIR and red edge bands, has been widely validated as a sensitive indicator of chlorophyll content, nitrogen status, and crop maturity for cotton (Khodjaev et al., 2024), it does not capture cotton's unique Red2 band behavior. By integrating both NDRE and Red2, RMCI captures complementary spectral characteristics of the two crops, thereby enhancing classification accuracy.

To further validate the effectiveness of RMCI in distinguishing between maize and cotton, the index was incorporated into the feature set for crop classification using the RF classifier. SHAP (Shapley Additive Explanations) values (Lundberg et al., 2018) were employed to assess the contribution of each input variable in predicting cotton presence. The results identified RMCI, VH, and NDRE as the three most influential predictors based on their mean absolute SHAP values (Fig. 12). RMCI consistently ranked among the top predictors on DOY 196, 181, and 211, underscoring its significance in distinguishing maize and cotton. Specifically, RMCI values on DOY 196 and 181 were the highest-ranking

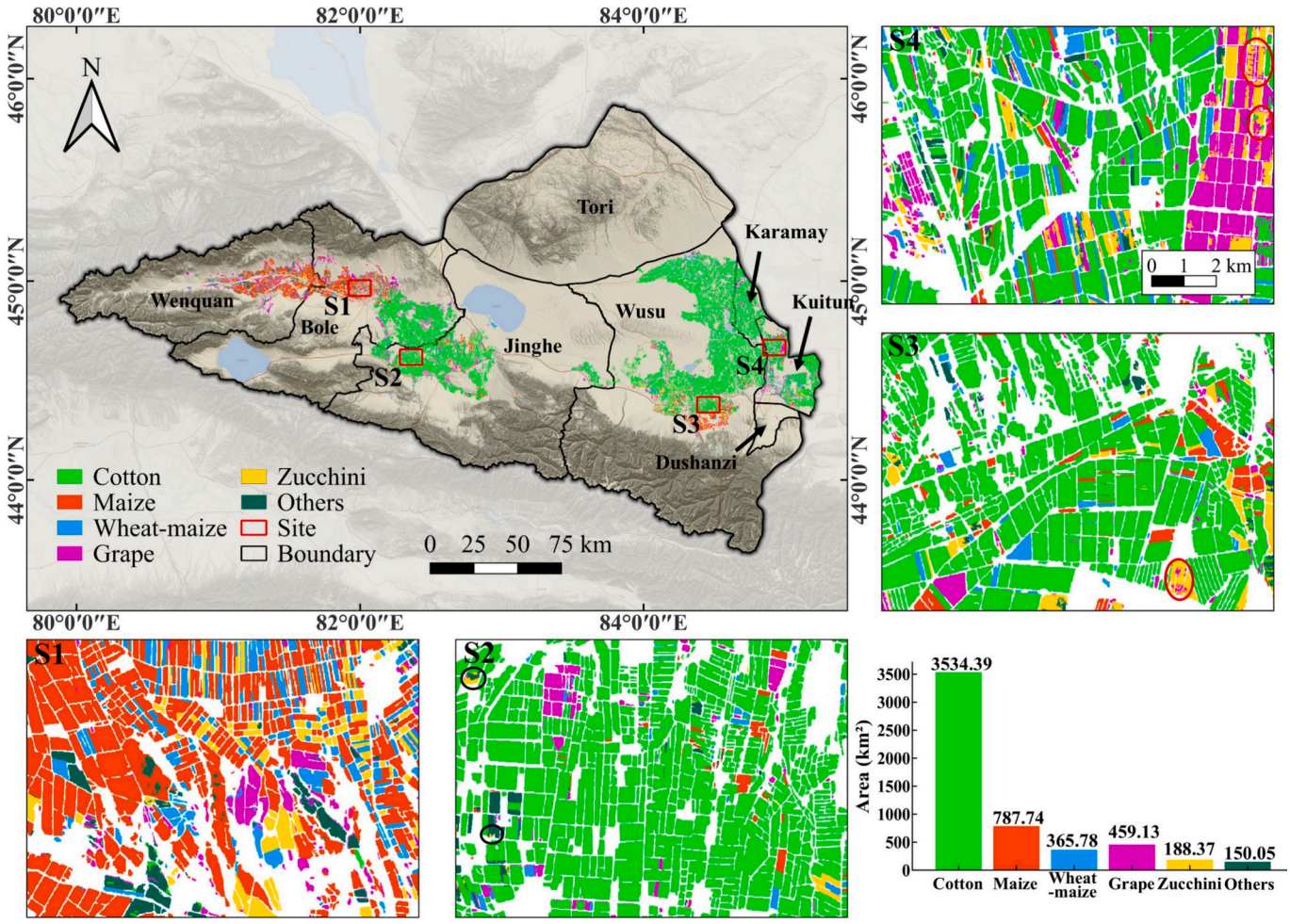


Fig. 11. Crop classification in the elb for 2023 using the hierarchical approach.

Table 4
Accuracy comparison between the hierarchical approach and the standalone RF classifier.

Approach	Cotton	Maize	Wheat-maize	Grape	Zucchini	Others
Hierarchical	99.04 %	97.44 %	88.24 %	92.66 %	94.38 %	92.31 %
Solely RF	97.28 %	96.22 %	81.97 %	89.01 %	75.61 %	88.89 %

variables, demonstrating its capacity to discriminate between the two crops as early as early July.

5.3. RMCI compared with previous studies

Several cotton-specific mapping indices have been developed, including the White Boll Index (WBI) by Wang et al. (2021) and the Cotton Mapping Index (CMI) by Xun et al. (2021). The WBI leverages Sentinel-2 imagery during the boll-opening stage to identify cotton. Compared to WBI, the RMCI offers simpler formulation and higher accuracy (98.6 % vs. 95.0 %). Similarly, RMCI outperforms CMI by providing a less complex calculation process while achieving superior mapping accuracy, with CMI's maximum OA reaching only 93.25 %. Existing cotton products in the ELB provide a benchmark for evaluation of RMCI transferability. Kang et al. (2023) employed an RF classifier to identify cotton in Xinjiang and mapped the distribution of cotton within the ELB in 2021. The ELB is characterized by a single dominant cropping season, with limited double-cropping practices (e.g., wheat–silage maize). Due to temperature-related constraints, the planting and phenological calendars of maize and cotton remain relatively consistent across years in ELB. Threshold, RMCI threshold in 2023 was directly applied to generate the cotton spatial distribution for 2021 in the ELB. Despite this simplification, the Fig. 13 shown that the classification results exhibit strong consistency and improved accuracy compared to those reported by Kang et al. (2023). Blue circles highlight areas where RMCI successfully identified cotton, while orange circles indicate regions where cotton was missed. Some discrepancies may be attributed to the use of a fixed inter-annual threshold, which may not have fully captured the peak growth stage (PGS) of cotton in 2021. In future work, it is necessary to develop dynamic or adaptive thresholding methods that better account for temporal and regional variations in crop growth stages and spectral responses.

5.4. Limitations and potential improvements

Although the hierarchical parcel-level crop classification method integrating RMCI and machine learning achieved good results in the ELB, some issues remain to be addressed in future studies. First, the RMCI threshold of 0.42 in 2023 was directly applied to 2021. Although satisfactory spectral separability was achieved in 2021, the potential

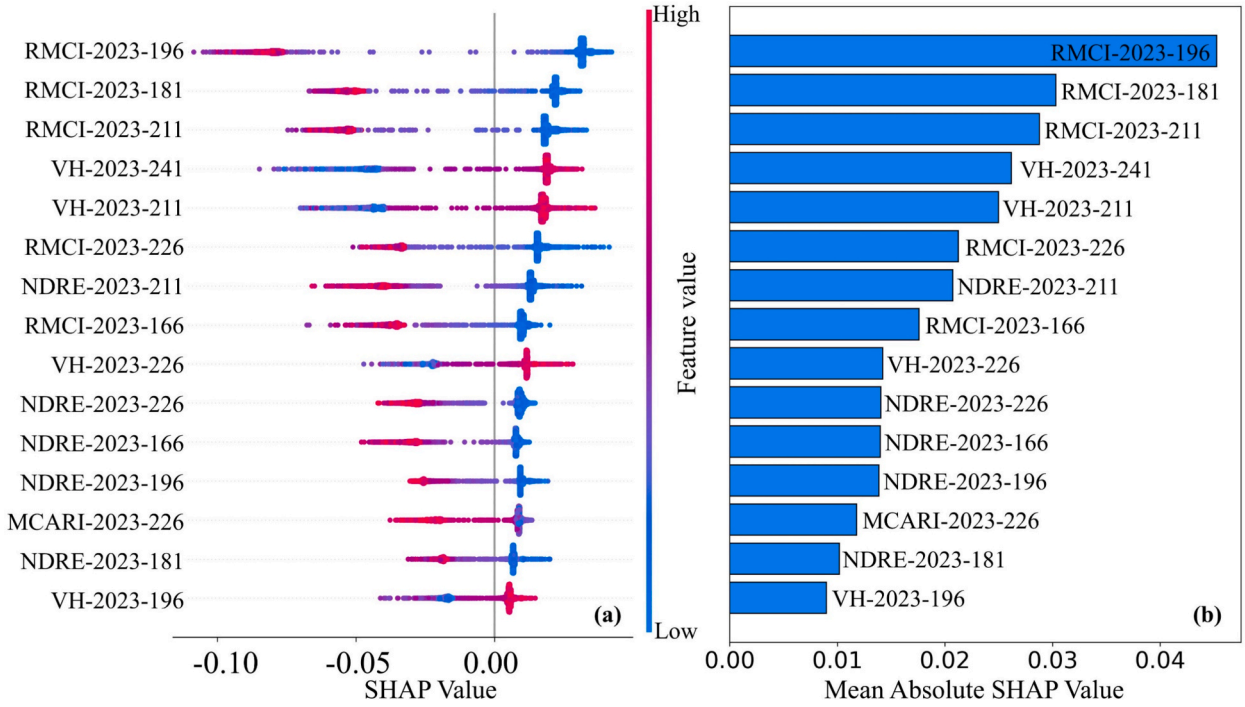


Fig. 12. The rank of SHAP values for the features. (a) The scatterplot illustrates the distribution of SHAP values for each variable, with the x-axis representing the SHAP value and the y-axis showing the variable name (which includes the index name, year, and DOY). (b) The bar graph displays the mean absolute SHAP values for each variable, indicating their overall importance in the model.

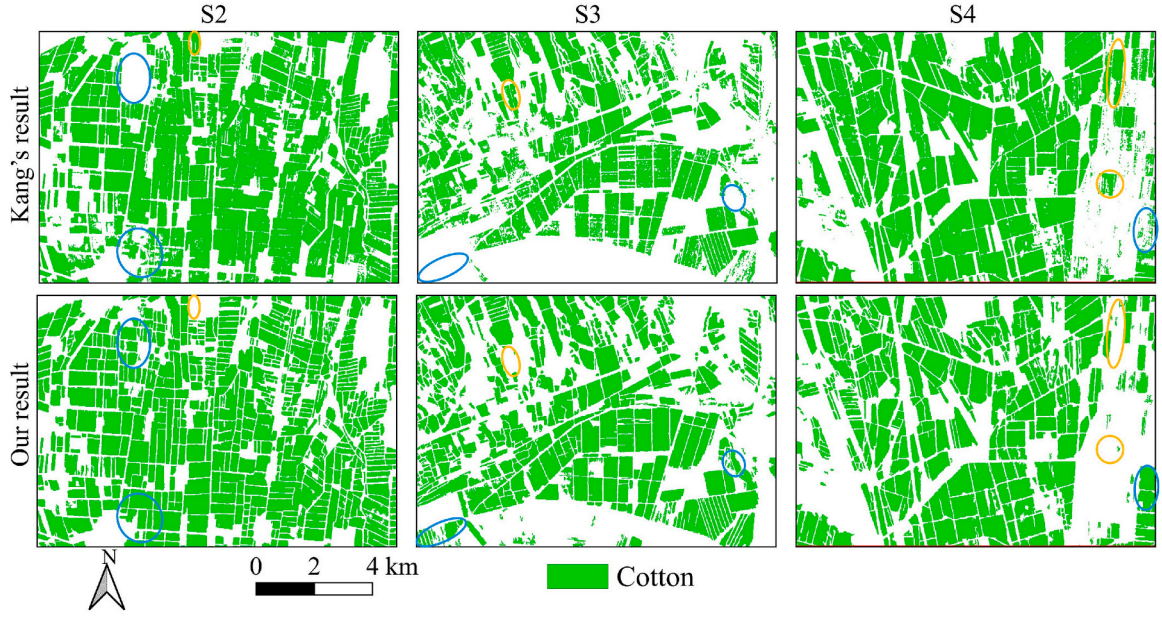


Fig. 13. The comparison of cotton distribution in 2021 derived from Kang et al. and the RMCI threshold-based approach. The location of sub-regions S2-S4 is consistent with those in Fig. 7.

impact of interannual phenological variation on threshold transferability should be systematically investigated in future research. Second, some minor crops, such as winter wheat-silage maize are underrepresented, which may affect classification performance by RF, to address the limited availability of labeled samples in the target region, a domain adaptation-based sample augmentation method could be employed to enhance model generalization in future. Third, the RMCI was specific designed for the separation of maize and cotton, if the dominant crop composition shifts, a new or existing crop-specific indices should be integrated into hierarchical crop classification, and the effectiveness should be explored more in future.

6. Conclusion

This study presented a hierarchical crop classification framework for the ELB that efficiently and accurately distinguished dominant crops (maize and cotton) while simultaneously classifying minor crops at parcel level. This framework integrated the strengths of index-based

methods for specific crops, machine learning-based methods for multi-crop classification, and cropland parcels for minimal 'pepper & salt' noise. BFINet delineated agricultural parcels in ELB with IOU of 82.3 % and OA of 87.8 %. A newly developed RMCI effectively separated maize and cotton, notably reducing the reliance on crop labels and achieving an OA of 98.6 %. The hierarchical framework outperformed the stand-alone RF classifier in classifying all crop types in the ELB. In addition, this study filled the gap in high-accuracy, parcel-level crop type maps in the ELB, providing valuable data support for water and food management. In summary, this study offered an improved classification strategy for multi-crops systems. Future work will evaluate the spatial and temporal transferability of RMCI and explore the integration of additional crop-sensitive indices to enhance its broader applicability.

CRediT authorship contribution statement

Yan Xie: Writing – original draft, Methodology, Investigation, Formal analysis, Data curation. **Hongwei Zeng:** Writing – review & editing, Supervision, Methodology, Formal analysis. **Junbin Li:** Writing – review & editing, Formal analysis. **Hang Zhao:** Writing – review & editing, Methodology. **Qiangyi Yu:** Writing – review & editing. **Bingwen Qiu:** Writing – review & editing. **Shukri Ahmed:** Writing – review & editing. **Bingfang Wu:** Writing – review & editing, Supervision.

Declaration of competing interest

The authors declare that they have no known competing financial interests or personal relationships that could have appeared to influence the work reported in this paper.

Acknowledgment

This research was financially supported by the National Natural Science Foundation of China (No. 42071271; No. 42471319).

Data availability

Data will be made available on request.

References

Abbasi, N., Hamideh, N., Pamela, N., Kamel, D., Sattar, C.B., Armando, B.-M., Christian, O., Siebert, S., 2023. Crop water use dynamics over arid and semi-arid croplands in the lower Colorado River Basin. Eur. J. Remote Sens. 56, 2259244.

Altman, N., Krzywinski, M., 2017. Ensemble methods: bagging and random forests. Nat. Methods 14, 933–934.

Asadi, B., Shamsoddini, A., 2024. Crop mapping through a hybrid machine learning and deep learning method. Remote Sens. Appl.: Soc. Environ. 33, 101090.

Cai, Z., Xu, B., Yu, Q., Zhang, X., Yang, J., Wei, H., Li, S., Song, Q., Xiong, H., Wu, H., Wu, W., Shi, Z., Hu, Q., 2024. A cost-effective and robust mapping method for diverse crop types using weakly supervised semantic segmentation with sparse point samples. ISPRS J. Photogramm. Remote Sens. 218, 260–276.

Chen, B., Jin, Y., Brown, P., 2019. An enhanced bloom index for quantifying floral phenology using multi-scale remote sensing observations. ISPRS J. Photogramm. Remote Sens. 156, 108–120.

d'Andrimont, R., Verhegghen, A., Lemoine, G., Kempeneers, P., Meroni, M., van der Velde, M., 2021. From parcel to continental scale – a first European crop type map based on Sentinel-1 and LUCAS Copernicus in-situ observations. Remote Sens. Environ. 266, 112708.

Defourny, P., Bontemps, S., Bellemans, N., Cara, C., Dedieu, G., Guzzonato, E., Hagolle, O., Inglada, J., Nicola, L., Rabaute, T., Savinaud, M., Udroiu, C., Valero, S., Bégué, A., Dejoux, J.-F., El Harti, A., Ezzahar, J., Kussul, N., Labbassi, K., Lebourgeois, V., Miao, Z., Newby, T., Nyamugama, A., Salh, N., Shelestov, A., Simonneaux, V., Traore, P.S., Traore, S.S., Koetz, B., 2019. Near real-time agriculture monitoring at national scale at parcel resolution: performance assessment of the Sen2-Agri automated system in various cropping systems around the world. Remote Sens. Environ. 221, 551–568.

Deines, J.M., Kendall, A.D., Crowley, M.A., Rapp, J., Cardille, J.A., Hyndman, D.W., 2019. Mapping three decades of annual irrigation across the US High Plains Aquifer using Landsat and Google Earth Engine. Remote Sensing of Environment 233.

Deng, Y., Wu, C., Li, M., Chen, R., 2015. RNDSI: a ratio normalized difference soil index for remote sensing of urban/suburban environments. Int. J. Appl. Earth Obs. Geoinf. 39, 40–48.

Diek, S., Fornallaz, F., Schaepman, M.E., De Jong, R., 2017. Barest pixel composite for agricultural areas using landsat time series. Remote Sens. (Basel).

Fung, T., Siu, W., 2010. Environmental quality and its changes, an analysis using NDVI. Int. J. Remote Sens. 21, 1011–1024.

Gorelick, N., Hancher, M., Dixon, M., Ilyushchenko, S., Thau, D., Moore, R., 2017. Google Earth Engine: planetary-scale geospatial analysis for everyone. Remote Sens. Environ. 202, 18–27.

Hirayama, H., Sharma, R.C., Mizuki, T., Hara, K., 2019. Evaluating multiple classifier system for the reduction of salt-and-pepper noise in the classification of very-high-resolution satellite images. Int. J. Remote Sens. 40, 2542–2557.

Hong, Y., Li, D., Wang, M., Jiang, H., Luo, L., Wu, Y., Liu, C., Xie, T., Zhang, Q., Jahangir, Z., 2022. Cotton cultivated area extraction based on multi-feature combination and CSSDI under spatial constraint. Remote Sens. (Basel) 14.

Huang, Y., Qiu, B., Yang, P., Wu, W., Chen, X., Zhu, X., Xu, S., Wang, L., Dong, Z., Zhang, J., 2024. National-scale 10 m annual maize maps for China and the contiguous United States using a robust index from Sentinel-2 time series. Comput. Electron. Agric. 221, 109018.

Huete, A.R., Didan, K., Miura, T., Rodriguez, E.P., Gao, X., Ferreira, L.G., 2002. Overview of the radiometric and biophysical performance of the MODIS vegetation indices. Remote Sens. Environ. 83, 195–213.

Kang, X., Huang, C., Chen, J.M., Lv, X., Wang, J., Zhong, T., Wang, H., Fan, X., Ma, Y., Yi, X., Zhang, Z., Zhang, L., Tong, Q., 2023. The 10-m cotton maps in Xinjiang, China during 2018–2021. Sci. Data 10, 688.

Khodjaev, S., Bobojonov, I., Kuhn, L., Glauben, T., 2024. An accuracy assessment of satellite-based cotton yield estimation using panel data regression: a case study of Uzbekistan. Environ. Dev. Sustain.

Kussul, N., Lavreniuk, M., Skakun, S., Shelestov, A., 2017. Deep learning classification of land cover and crop types using remote sensing data. IEEE Geosci. Remote Sens. Lett. 14, 778–782.

Li, M., Long, J., Stein, A., Wang, X., 2023. Using a semantic edge-aware multi-task neural network to delineate agricultural parcels from remote sensing images. ISPRS J. Photogramm. Remote Sens. 200, 24–40.

Lian, X., Piao, S., Chen, A., Wang, K., Li, X., Buermann, W., Huntingford, C., Peñuelas, J., Xu, H., Myneni, R.B., 2021. Seasonal biological carryover dominates northern vegetation growth. Nat. Commun. 12, 983.

Long, J., Li, M., Wang, X., Stein, A., 2022. Delineation of agricultural fields using multi-task BsiNet from high-resolution satellite images. Int. J. Appl. Earth Obs. Geoinf. 112.

Lundberg, S.M., Erion, G.G., Lee, S.-I., 2018. Consistent individualized feature attribution for tree ensembles. ArXiv abs/1802.03888.

Ma, X., Zhu, J., Zhang, H., Yan, W., Zhao, C., 2020. Trade-offs and synergies in ecosystem service values of inland lake wetlands in Central Asia under land use/cover change: a case study on Ebinur Lake, China. Global Ecol. Conserv. 24, e01253.

Merzlyak, M.N., Gitelson, A.A., Chivkunova, O.B., Rakitin, V.Y.U., 2002. Non-destructive optical detection of pigment changes during leaf senescence and fruit ripening. Physiol. Plant. 106, 135–141.

Mullissa, A., Vollrath, A., Odongo-Braun, C., Slagter, B., Balling, J., Gou, Y., Gorelick, N., Reiche, J., 2021. Sentinel-1 SAR backscatter analysis ready data preparation in Google Earth Engine. Remote Sens. (Basel) 13.

Nagler, P., Daughtry, C., Goward, S., 2000. Plant litter and soil reflectance. Remote Sens. Environ. 71, 207–215.

Pagani, A., Echeverría, H.E., Andrade, F.H., Rozas, H.S., 2009. Characterization of corn nitrogen status with a greenness index under different availability of sulfur. Agron. J. 101, 315–322.

Pedregosa, F., Varoquaux, G., Gramfort, A., Michel, V., Thirion, B., Grisel, O., Blondel, M., Prettenhofer, P., Weiss, R., Dubourg, V., Vanderplas, J., Passos, A., Cournapeau, D., Brucher, M., Perrot, M., Duchesnay, É., 2011. Scikit-learn: machine learning in Python. J. Mach. Learn. Res. 12, 2825–2830.

Shafizadeh-Moghadam, H., Khazaei, M., Alavipanah, S.K., Weng, Q., 2021. Google Earth Engine for large-scale land use and land cover mapping: an object-based classification approach using spectral, textural and topographical factors. Gisci. Remote Sens. 58, 914–928.

Shen, Y., Zhang, X., Yang, Z., 2022. Mapping corn and soybean phenometrics at field scales over the United States Corn Belt by fusing time series of Landsat 8 and Sentinel-2 data with VIIRS data. ISPRS J. Photogramm. Remote Sens. 186, 55–69.

Shi, G., Du, X., Du, M., Li, Q., Tian, X., Ren, Y., Zhang, Y., Wang, H., 2022. Cotton yield estimation using the remotely sensed cotton boll index from UAV images. Drones 6.

Sims, D.A., Gamon, J.A., 2002. Relationships between leaf pigment content and spectral reflectance across a wide range of species, leaf structures and developmental stages. Remote Sens. Environ. 81, 337–354.

Sonnentag, O., Hufkens, K., Teshera-Sterne, C., Young, A.M., Friedl, M., Braswell, B.H., Milliman, T., O'Keefe, J., Richardson, A.D., 2012. Digital repeat photography for phenological research in forest ecosystems. Agric. For. Meteorol. 152, 159–177.

Tan, C.P., Ewe, H.T., Chuah, H.T., 2011. Agricultural crop-type classification of multi-polarization SAR images using a hybrid entropy decomposition and support vector machine technique. Int. J. Remote Sens. 32, 7057–7071.

Tian, Y., Shuai, Y., Shao, C., Wu, H., Fan, L., Li, Y., Chen, X., Narimanov, A., Usmanov, R., Baboeva, S., 2023. Extraction of cotton information with optimized phenology-based features from Sentinel-2 images. Remote Sens. (Basel) 15.

Veloso, A., Mermoz, S., Bouvet, A., Le Toan, T., Planells, M., Dejoux, J.-F., Ceschia, E., 2017. Understanding the temporal behavior of crops using Sentinel-1 and Sentinel-2-like data for agricultural applications. Remote Sens. Environ. 199, 415–426.

Wang, N., Zhai, Y., Zhang, L., 2021. Automatic cotton mapping using time series of Sentinel-2 images. Remote Sens. (Basel) 13.

Wang, Y., Feng, L., Sun, W., Wang, L., Yang, G., Chen, B., 2024. A lightweight CNN-Transformer network for pixel-based crop mapping using time-series Sentinel-2 imagery. Comput. Electron. Agric. 226, 109370.
Wang, Y., Feng, L., Zhang, Z., Tian, F., 2023. An unsupervised domain adaptation deep learning method for spatial and temporal transferable crop type mapping using Sentinel-2 imagery. ISPRS J. Photogramm. Remote Sens. 199, 102–117.
Worrall, G., Judge, J., Boote, K., Rangarajan, A., 2023. In-season crop phenology using remote sensing and model-guided machine learning. 115, 1214–1236.
Wu, B., Fu, Z., Fu, B., Yan, C., Zeng, H., Zhao, W., 2024. Dynamics of land cover changes and driving forces in China's drylands since the 1970 s. Land Use Policy 140.
Wu, B., Li, Q., 2012. Crop planting and type proportion method for crop acreage estimation of complex agricultural landscapes. Int. J. Appl. Earth Obs. Geoinf. 16, 101–112.
Wu, C., Niu, Z., Tang, Q., Huang, W., 2008. Estimating chlorophyll content from hyperspectral vegetation indices: modeling and validation. Agric. For. Meteorol. 148, 1230–1241.
Xiao, X., Boles, S., Frolking, S., Salas, W., Moore, B., Li, C., He, L., Zhao, R., 2010. Observation of flooding and rice transplanting of paddy rice fields at the site to landscape scales in China using VEGETATION sensor data. Int. J. Remote Sens. 23, 3009–3022.
Xu, S., Zhu, X., Chen, J., Zhu, X., Duan, M., Qiu, B., Wan, L., Tan, X., Xu, Y.N., Cao, R., 2023. A robust index to extract paddy fields in cloudy regions from SAR time series. Remote Sens. Environ. 285.
Xuan, F., Dong, Y., Li, J., Li, X., Su, W., Huang, X., Huang, J., Xie, Z., Li, Z., Liu, H., Tao, W., Wen, Y., Zhang, Y., 2023. Mapping crop type in Northeast China during 2013–2021 using automatic sampling and tile-based image classification. Int. J. Appl. Earth Obs. Geoinf. 117, 103178.
Xun, L., Zhang, J., Cao, D., Yang, S., Yao, F., 2021. A novel cotton mapping index combining Sentinel-1 SAR and Sentinel-2 multispectral imagery. ISPRS J. Photogramm. Remote Sens. 181, 148–166.
Yang, G., Li, X., Liu, P., Yao, X., Zhu, Y., Cao, W., Cheng, T., 2023. Automated in-season mapping of winter wheat in China with training data generation and model transfer. ISPRS J. Photogramm. Remote Sens. 202, 422–438.
You, N., Dong, J., Huang, J., Du, G., Zhang, G., He, Y., Yang, T., Di, Y., Xiao, X., 2021. The 10-m crop type maps in Northeast China during 2017–2019. Sci. Data 8, 41.
Zeng, H., Wu, B., Wang, S., Musakwa, W., Tian, F., Mashimbye, Z.E., Poona, N., Syndey, M., 2020. A synthesizing land-cover classification method based on Google Earth Engine: a case study in Nzhelele and Levhuvu Catchments, South Africa. Chin. Geogr. Sci. 30, 397–409.
Zeng, H., Xie, Y., Elnashar, A., Wang, S., Zhao, H., Li, J., Wu, B., 2025. Increasing cropland area and its associated human-induced water consumption put Ebinur Lake at risk of drying up. J. Remote Sens. 5, 0496.
Zhang, C., Di, L., Lin, L., Li, H., Guo, L., Yang, Z., Yu, E.G., Di, Y., Yang, A., 2022. Towards automation of in-season crop type mapping using spatiotemporal crop information and remote sensing data. Agr. Syst. 201, 103462.
Zhang, L., Zhang, Y., Yin, X., 2023. Aquarius sea surface salinity retrieval in coastal regions based on deep neural networks. Remote Sens. Environ. 284.
Zhang, X., Cai, Z., Hu, Q., Yang, J., Wei, H., You, L., Xu, B., 2024. Improving crop type mapping by integrating LSTM with temporal random masking and pixel-set spatial information. ISPRS J. Photogramm. Remote Sens. 218, 87–101.
Zhang, Z., Wei, J., Yang, X., Sang, Z., 2013. Dry matter production and resources use efficiency of double-cropping winter wheat-forage maize system in North Xinjiang. Agric. Res. Arid Areas. 31, 28–33.
Zhao, H., Long, J., Zhang, M., Wu, B., Xu, C., Tian, F., Ma, Z., 2024. Irregular agricultural field delineation using a dual-branch architecture from high-resolution remote sensing images. IEEE Geosci. Remote Sens. Lett. 21, 1–5.
Zhao, H., Wu, B., Zhang, M., Long, J., Tian, F., Xie, Y., Zeng, H., Zheng, Z., Ma, Z., Wang, M., Li, J., 2025. A large-scale VHR parcel dataset and a novel hierarchical semantic boundary-guided network for agricultural parcel delineation. ISPRS J. Photogramm. Remote Sens. 221, 1–19.
Zhong, L., Hu, L., Zhou, H., 2019. Deep learning based multi-temporal crop classification. Remote Sens. Environ. 221, 430–443.
Zhu, X., 2013. Land cover classification using moderate resolution satellite imagery and random forests with post-hoc smoothing. J. Spat. Sci. 58, 323–337.